


Article

Model Test Study on Bearing Capacity and Deformation Characteristics of Symmetric Pile–Bucket Foundation Subjected to Cyclic Horizontal Load

Zunan Fu ¹, Guoshuai Wang ¹, Yanming Yu ¹ and Li Shi ^{2,*} 
¹ Huadong Engineering Corporation Limited, Hangzhou 311122, China; fu_zn@hdec.com (Z.F.); wang_gs@hdec.com (G.W.); yu_ym@hdec.com (Y.Y.)

² College of Civil Engineering, Zhejiang University of Technology, Hangzhou 310014, China

* Correspondence: lishi@zjut.edu.cn

Abstract: The pile–bucket foundation that features a bucket slipped onto a monopile is a new type of symmetric offshore foundation supporting the wind turbine. Its load bearing and deformation resistance capacity are unclear, especially when subjected to cyclic horizontal loadings. In this paper, a model test has been designed and carried out for investigating the cyclic behavior of the pile–bucket foundation embedded in soft marine clay. Cyclic horizontal loads are applied in a displacement-controlled manner with different amplitudes and frequencies. The influences of cyclic loading parameters, including the amplitude, the frequency and the cycle number, have been studied from the perspectives of stiffness-degradation and damping effect that are evaluated from the recorded horizontal force–displacement relationships at the loading point. In addition, the influences of cyclic horizontal loading on the bending moment distribution and on the p – y curve have been presented and discussed. The results show that significant reductions in the foundation stiffness and in the soil resistance may be observed during the first few cycles when the loading displacement is relatively high.

Keywords: pile–bucket foundation; model test; horizontal cyclic loading; secant stiffness; soil resistance



Citation: Fu, Z.; Wang, G.; Yu, Y.; Shi, L. Model Test Study on Bearing Capacity and Deformation Characteristics of Symmetric Pile–Bucket Foundation Subjected to Cyclic Horizontal Load. *Symmetry* **2021**, *13*, 1647. <https://doi.org/10.3390/sym13091647>

Academic Editors: Raffaele Barretta and Sergei D. Odintsov

Received: 8 August 2021

Accepted: 2 September 2021

Published: 7 September 2021

Publisher's Note: MDPI stays neutral with regard to jurisdictional claims in published maps and institutional affiliations.



Copyright: © 2021 by the authors. Licensee MDPI, Basel, Switzerland. This article is an open access article distributed under the terms and conditions of the Creative Commons Attribution (CC BY) license (<https://creativecommons.org/licenses/by/4.0/>).

1. Introduction

As a clean and renewable energy source, offshore wind energy has been attracting more and more attention all over the world. At present, commonly used offshore wind-turbine foundations mainly include the gravity foundation, the jacket foundation, the bucket foundation and the monopile foundation [1], among which the monopile foundation has become more welcomed especially in soft soil areas owing to its simple structure, easy installation and relatively high reliability. To ensure the working conditions of the wind turbine, stringent requirements surrounding the cumulative deformation of the foundation should be met. Thus, for monopiles in soft marine soil, there is a continuous need to improve the deformation resistance capacity even though monopiles of high rigidity (e.g., with diameter as large as 6–8 m) have been used in practice. To this aim, a new type of offshore foundation that combines the bucket and monopile, i.e., the so-called pile–bucket foundation, has been proposed and successfully used in windfarm practices of southeastern China, see Figure 1. It is of vital importance to understand the load-bearing and deformation-resistance characteristics of this new foundation when it is subjected to horizontal wind/wave loads.

As an integrated part of the pile–bucket foundation, the monopile has been studied intensively using both numerical, analytical and field/model test methods. Here we focus on the model tests on the monopile foundation when subjected to either monotonic or cyclic horizontal loadings. Based on direct measurements of the soil–pile interaction pressure and the lateral pile displacement, Suleiman et al. [2] developed the direct measurement-based

p - y curves. Li et al. [3] conducted a series of lateral load tests on reduced-scale monopiles in over-consolidated dense sand to investigate the influence of shear force on the lateral behavior of monopiles. A centrifuge test was performed by Yu et al. [4] to investigate the ultimate lateral capacity of a free-head rigid monopile foundation in normally consolidated clay. Zou et al. [5] carried out several laboratory studies to explore the effects of water flow on the lateral response of monopiles in sand.

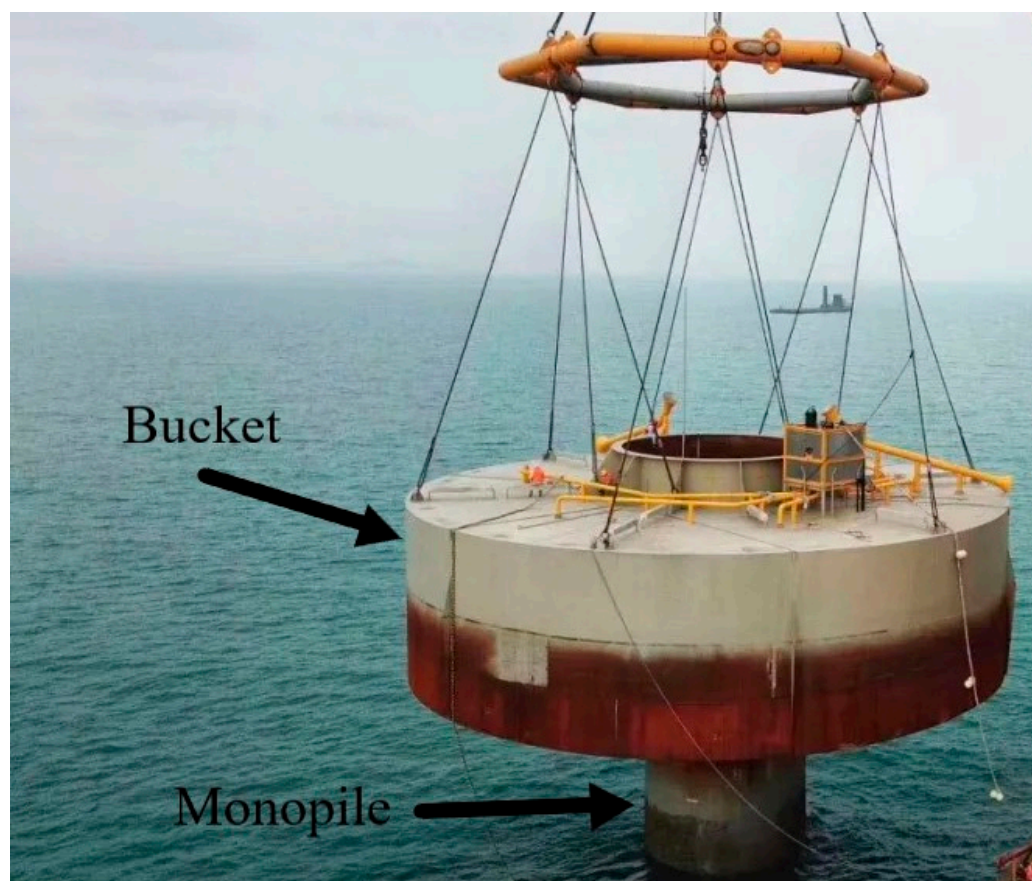


Figure 1. Field photo of pile–bucket foundation.

For cyclic horizontal loadings, Leblanc et al. [6] conducted a series of small-scale tests on driven piles to explore the effects of cyclic loading pattern, cyclic loading number and cyclic loading range on the cumulative lateral displacement of piles. Zhang et al. [7] performed a series of centrifuge model tests to study the cyclic lateral response of a rigid pile in soft soil and found that with the increasing cyclic loading time the pile lateral stiffness may approach a constant independent of the number of cycles. Lombardi et al. [8] carried out several laboratory tests on a scaled monopile model in kaolin clay to explore the long-term cyclic characteristics of offshore wind turbines, such as changes in natural frequency and damping. A group of centrifuge tests was performed by Yu et al. [9] to study the effect of soil liquefaction under seismic motion on the stability of the monopile. More recently, Hong et al. [10] investigated the cyclic lateral response and failure mechanisms of a semi-rigid pile in soft clay through a series of centrifuge model tests. Using a newly designed loading device, Liao et al. [11] performed several scaled model tests to investigate the cyclic lateral behavior of monopiles constructed in intertidal zones. A series of centrifuge tests were performed by Lai et al. [12] to simulate the effects of episodic cycling and soil reconsolidation on the cyclic lateral behavior of large-diameter monopiles. Jawad et al. [13] performed six reduced-scale model tests on a monopile to investigate its cyclic behavior. The above-mentioned model test work on the monopile foundation is summarized in Table 1 including details of the model scales and the soil types.

Table 1. Summary on existing model test studies on laterally loaded monopile foundations.

Reference	Model Scale	Test Type	Loading Type	Soil Type
Leblanc et al. (2010)	1:50	1 g ¹	Cyclic	Sand
Zhang et al. (2011)	1:50	N g ²	Cyclic	Kaolin Clay
Lombardi et al. (2013)	1:56	1 g	Cyclic	London Clay
Suleiman et al. (2015)	1:1	1 g	Monotonic	Sand
Yu et al. (2015)	1:50	N g	Cyclic	Toyoura sand
Hong et al. (2016)	1:40	N g	Cyclic	Soft Clay
Li et al. (2017)	1:18	1 g	Monotonic	Dense sand
Yu et al. (2017)	1:50	N g	Monotonic	Kaolin Clay
Liao et al. (2018)	1:100	1 g	Cyclic	Marine clay
Lai et al. (2020)	1:100	N g	Cyclic	Soft Clay
Jawad et al. (2021)	1:6	1 g	Both cyclic and monotonic	Kansas River Sand
Zou et al. (2021)	1:100	1 g	Monotonic	Medium silica sand

¹ 1 g denotes normal gravity condition; ² N g denotes N times the normal gravity.

As another integrated component of the pile–bucket foundation, the suction bucket has also gained lots of attention. The current understanding of the bearing capacity of a laterally loaded suction bucket foundation has mainly been obtained through model tests. Wang et al. [14] conducted a series of centrifuge tests on a suction bucket foundation in sand to study the lateral bearing capacity. With considerations of different loading heights, Zhu et al. [15] conducted large-scale model tests to investigate the position of the instantaneous rotation center and the distribution of soil pressures. Based on the model test results, an analytical approach for determining the ultimate moment capacity of the suction bucket was proposed. Based on the force equilibrium analysis of the bucket, Zhu et al. [16] proposed a new calculation method on the deflection-based bearing capacity.

Due to the uninterrupted loads generated by wind and wave, the cyclic behavior of a laterally loaded bucket foundation over its design life needs to be understood. Ma et al. [17] studied the lateral bearing response of the shallow bucket foundation under a dynamic cyclic load. Cox et al. [18] conducted a series of centrifuge tests on a cyclically loaded suction bucket foundation in sand by considering different aspect ratios of the bucket. The variation in stiffness of the caisson is found to be related to the amplitude of cyclic moment loading [19]. The rotation accumulation of laterally loaded suction caisson foundations in sand has been extensively studied ([18,20,21]). It was found that the cumulative rotation follows a power relationship with respect to the loading cycles. Zhu et al. [22,23] performed model tests on the bucket foundation with due considerations on the clay soil and on the symmetrical cyclic load conditions. The effect of variation in the direction of cyclic loading on the responses of the bucket foundation has also been investigated by Zhu et al. [24].

Considering the above, deep insights into the loading bearing and deformation resistance capacities have been gained for the monopile and bucket foundations, respectively, using model test methods. However, as a new type of foundation, the existing work on the pile–bucket foundation is somehow limited. Chen et al. [25] investigated the static and dynamic loading behaviors of this new type of foundation using the finite element method. Both static and dynamic responses reveal that the bucket can effectively restrain the deformation, i.e., rotation and lateral displacement of the foundation. Currently, there has been no report on the model testing of the pile–bucket foundation.

To this end, a large-scale model test is designed and performed to investigate the horizontal load-bearing and deformation-resistance characteristics of the pile–bucket foundation that is embedded in soft marine clay. Three test cases have been carried out, including a monotonic horizontal loading case, a cyclic loading case with stepped-increasing displacement amplitudes and a cyclic loading case with stepped-increasing cycling frequencies. Test results are presented both as directly measured data (the loading force and displacement at the loading point) and the deduced quantities including the bending moment and the soil resistance. Discussions have been made, and conclusions have been

drawn on the load-bearing and deformation-resistance characteristics of the pile–bucket foundation when subjected to the cyclic horizontal loading.

2. Model Test Setup

2.1. Model Box

A model box of dimensions 2 m (length) \times 2 m (width) \times 3 m (height) is designed and manufactured specifically for testing the pile–bucket foundation, as shown in Figure 2a. On top of the box, there is the pile driving device that can help with pressing the model pile into the soil. Additionally, there is a reaction beam at the top, on which a servo-loading device is mounted to apply the required horizontal loading. The loading device is equipped with an LVDT (Linear Variable Differential Transformer) such that the loading force together with the loading displacement can be simultaneously recorded for the entire loading process. To accelerate the seepage consolidation of the test soil, PVDs (Prefabricated Vertical Drain) are attached to the inside wall of the model box. The PVD tip is buried into the drainage system at the bottom of the box, composed of layers of gravel, fine sand and permeable geotextile (from bottom to up). The pile-driving, horizontal-loading and the drainage systems are schematically shown in Figure 2b.

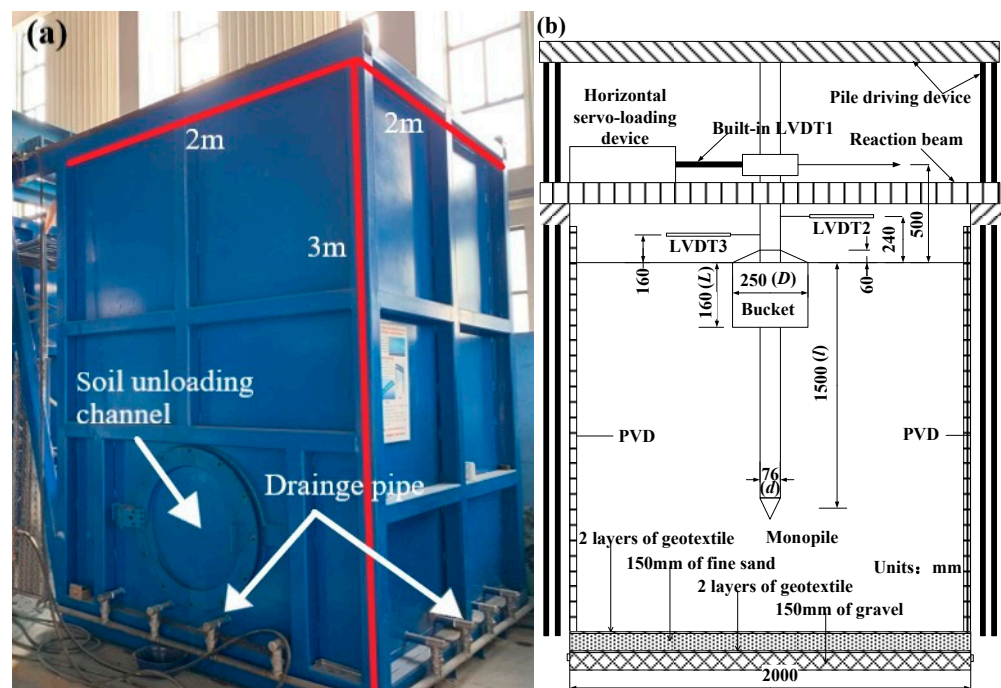


Figure 2. Model test system configurations: (a) picture of model box; (b) schematic view on model box components.

2.2. Test Soil

The test soil is sampled from a land reclamation site that is formed by dredging the seabed soil into the cofferdam at a coastal city of eastern China. The particle size distribution of the test soil is shown in Figure 3, from which the mass contents of clay, silt and sand particles can be read as 39%, 58% and 3%, respectively. Together with the determined liquid limit ($w_l = 37\%$), plastic limit ($w_p = 18\%$), and the plastic index ($I_p = 19$), the test soil can be classified as low-plasticity clay according to the unified soil classification system [26].

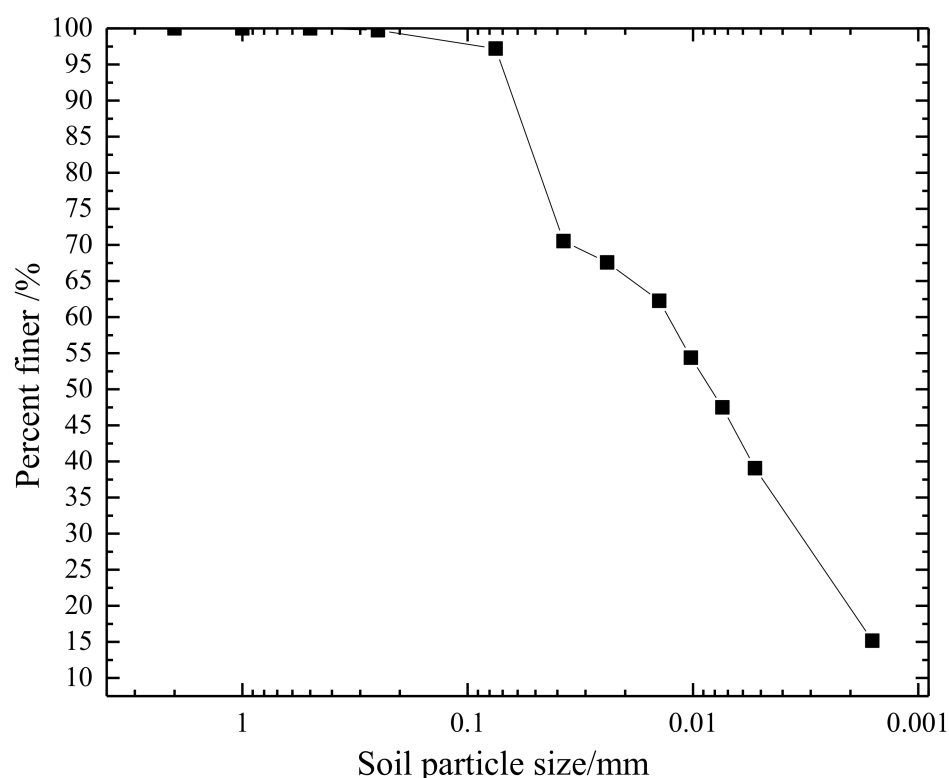


Figure 3. Particle size distribution of test soil.

After filling the test soil into the model box to an approximate height of 3 m, the soil is covered by a membrane to prevent water evaporation, and then left for rest for about 90 days. Following this, the steel plate together with the concrete block on top of it are loaded onto the surface of the soil to start the seepage consolidation. The total preloading pressure exerted by the steel plate and the concrete block is 20 kPa. Soil settlement is recorded for the preloading duration, as shown in Figure 4. The preloading pressure is removed when the settlement rate becomes less than 1 mm/week. From Figure 4, the degree of consolidation of the test soil at the end of the preloading can be estimated as 93%.

Then, the micro-vane shear test is performed along the central line of the model box to determine the variation of the undrained shear strength along the depth, as shown in Figure 5. It is read from the figure that the strength varies from about 8 kPa to 23 kPa, which falls in the typical range of undrained shear strength of soft marine soil.

2.3. Model Pile and Bucket

The relative bending stiffness of the pile is the dominating scaling factor when the prototype foundation is scaled down to the model test of this paper. Specifically, the material and the geometric properties of the model pile and bucket are determined such that the pile–soil stiffness ratio k_R [27] of the model falls into the semi-rigid category, as required by the general design practice for the prototype large-diameter pile foundations. The scaling factor of the length dimension is then determined to be 1:40 in the present paper. Scaling factors for various physical quantities between the prototype and the model foundations are summarized in Table 2. Accordingly, the dimensions of the hollow model pile are determined as 2500 mm in length, 76 mm in diameter and 3 mm in wall thickness. The pile tip is closed by a cone of height 40 mm. As for the model bucket, it is composed of the hoops, the ribs, the cover plate and the skirt. The skirt is 160 mm in height and 250 mm in outer diameter. The hoop is of height 60 mm and inner diameter 76 mm. The circular cover plate is of diameter 250 mm. The triangle-shaped rib of height 60 mm and length 84 mm strengthens the connection between the cover plate and the hoop. The geometrical dimensions of the model pile and bucket are indicated in Figure 2b. The

model pile and bucket are both manufactured using SUS304 steel, and photos of them are presented in Figure 6.

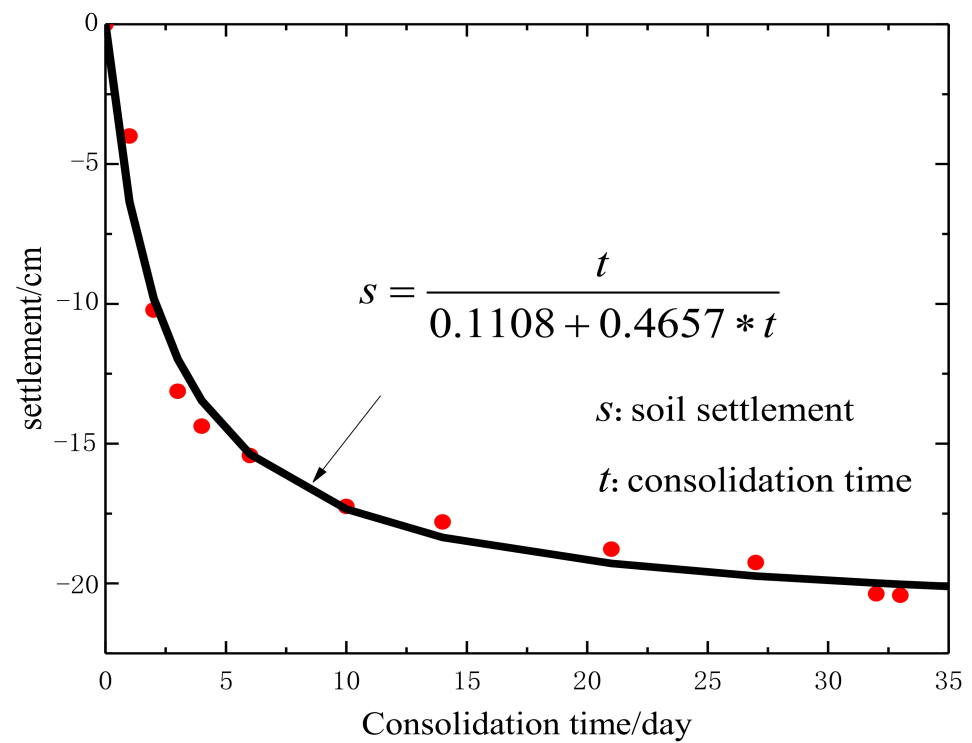


Figure 4. Settlement of soil recorded at the surface.

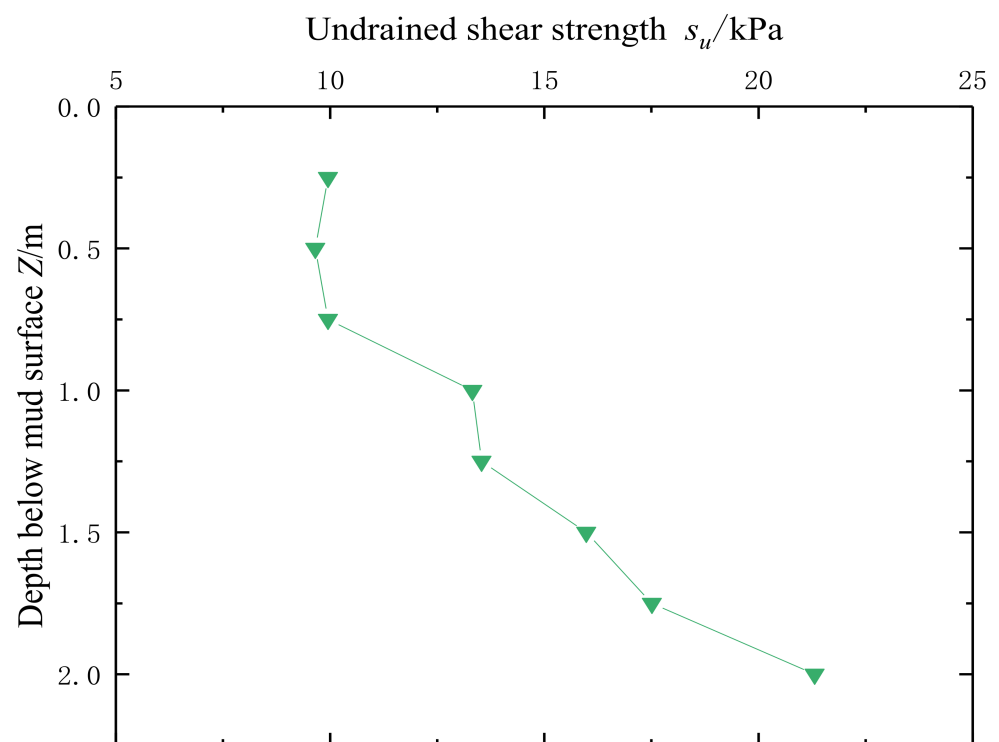
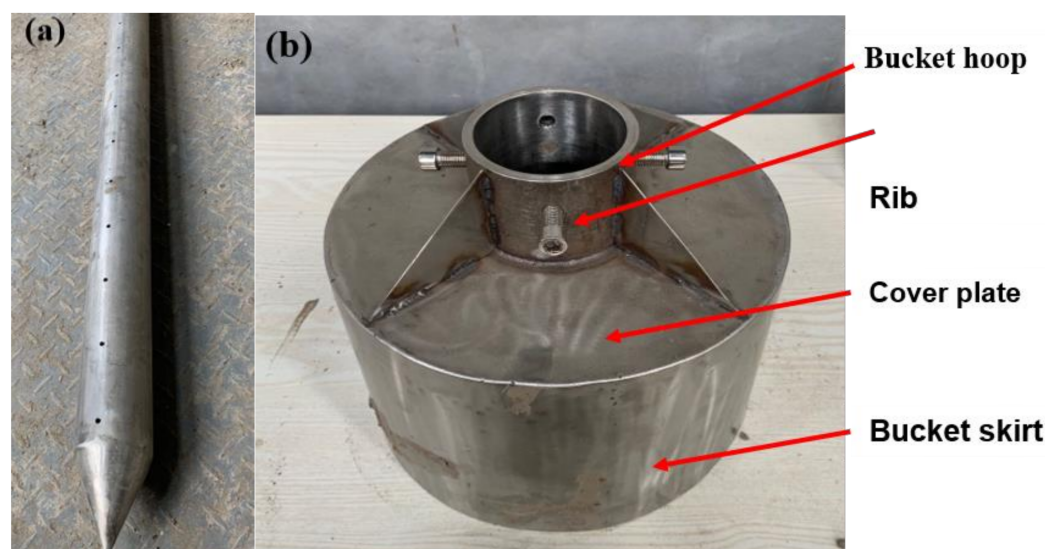


Figure 5. Variation of undrained shear strength of test soil along the depth.

Table 2. Scaling factors between the model and the prototype foundations.

Physical Quantity	Scaling Factor (Model/Prototype)
Bending stiffness	1:N ⁴
Length	1:N
Force	1:N ³
Gravitational acceleration	1:1

**Figure 6.** Photos of components of the model pile–bucket foundation: (a) model pile; (b) model bucket.

The model bucket is slipped onto the model pile and then fixed by bolts connecting the hoop to the pile shaft, as shown in Figure 6b. However, the bolt does not screw into the pile shaft after its penetration of the hoop. Instead, the bolt end clings onto the pile shaft under the bolting pressure. In this way, the over-rigid connection between the pile and the bucket can be avoided such that the model pile–bucket foundation would better resemble the cast-in-place concrete connection for the prototype.

Twenty pairs of strain gages have been arranged along the pair shaft with one pair located 160 mm above the cover plate of the bucket and the remaining 19 pairs below it at a spacing of 80 mm, as schematically shown in Figure 7. For each pair, the two gages are connected according to the half-bridge method. Two additional LVDTs are arranged at 160 mm and 240 mm above the cover plate to record the horizontal displacement of the pile shaft, as shown in Figure 2b.

Even though the model pile is made by a standard SUS304 steel tube, its bending rigidity has to be calibrated using the cantilever beam method, since small holes have to be punched on the shaft to lead out the wires of the gages. The calibrated bending rigidity $E_p I_p$ of the model pile is 89.06 kN·m². Then the pile–soil stiffness ratio $k_R = E_p I_p / E_s / l^4$ that is commonly adopted to classify the horizontal pile behavior can be determined as $k_R = 0.0107$, which falls into the semi-rigid category ($0.0025 < k_R < 0.208$) [27]. $E_s = 2.5$ MPa is the secant modulus of the test soil, which is determined by sampling the consolidated soil and then performing the undrained compression test to obtain the variation of the deviator stress over the axial strain. At the same time, the soil strain ε_c at one-half of the maximum deviator stress can be determined as $\varepsilon_c = 2\%$. The embedding depth of the model pile, $l = 1.5$ m.

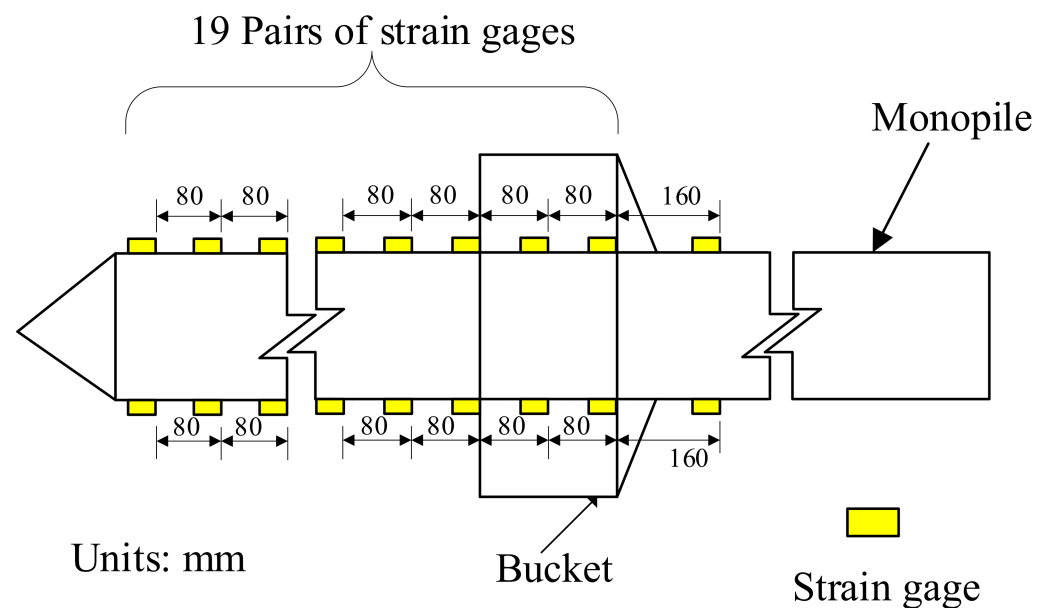


Figure 7. Schematic view of the distribution of strain gages on the model pile.

2.4. Test Operation Procedure

- (1) Cover the mud surface with a thin layer of water to ensure saturation of the soil during the test;
- (2) Arrange the strain gages along the model pile and lead the gage wires into the hollow cylinder of the pile through the punched holes on the pile shaft. Slip the model bucket onto the model pile and then connect them by the bolts such that the cover plate of the bucket is 1000 mm below the pile top;
- (3) Locate the model pile–bucket foundation near the center of the model box. Since the ratio between the box width (2 m) and the bucket diameter (250 mm) is 8 and is sufficiently larger than the immediate influence area of the foundation, the adverse influence of the model boundary can be avoided;
- (4) Start the installation by using the pile driving device. The driving rate is controlled to 100 mm/min to minimize the soil disturbance. The verticality of the pile during the driving process is ensured with the aid of a level meter. The driving is stopped when the cover plate of the bucket is at the mud surface.
- (5) Install the LVDTs and connect all the wires to the data logger connecting to a computer. Initialize the horizontal servo-loading device and set the loading height to 500 mm above the mud surface;
- (6) Let the model setup rest for 30 days to allow for regaining of soil strength that was disturbed during the pile driving. Then start the horizontal loading in a displacement-controlled manner.
- (7) The above steps are repeated for each test case that are detailed in the next section.

3. Test Cases

Before the cyclic loading, the pile–bucket foundation is monotonically loaded by the horizontal servo-loading device to obtain the force–displacement relationship at the load point, from which the ultimate bearing capacity F_u of the foundation can be obtained. Then, we start a new test to apply the bi-directional cyclic displacement to the loading point. The cyclic displacement is in the form of a sine wave of amplitude A and frequency f . Two cyclic loading cases have been considered, i.e., the first is of fixed frequency $f = 0.5$ Hz and of stepped increasing amplitude $A = \pm 5, \pm 10, \pm 20, \pm 25$ and ± 30 mm; while the latter is of fixed amplitude $A = \pm 2.5$ mm and of stepped increasing frequency $f = 0.1, 0.3$ and 0.5 Hz. For each combination of A and f , 100 loading cycles are applied. The test cases are summarized in Table 3. It is noted that the considered frequencies, i.e., $f = 0.1, 0.3$ and

0.5 Hz, are the typical loading frequencies of energy rich waves [28]. Furthermore, the force outputs at all the considered displacement amplitudes are within the ultimate bearing capacity F_u of the model foundation, as will be shown later.

Table 3. Test cases on model pile–bucket foundation.

Case No.	Case Description	Frequency f /Hz	Amplitude A /mm	Cycle Number
1	Monotonic loading		monotonic	
			± 5	
			± 10	
2	Cyclic loading with stepped increasing amplitudes	0.5	± 20	100
			± 25	
			± 30	
	Cyclic loading with stepped increasing frequency	0.1		
3		0.3	± 2.5	100
		0.5		

To facilitate the description, two additional parameters [6] $\zeta_b = F_{\max}/F_u$ and $\zeta_c = F_{\min}/F_{\max}$ are introduced to characterize the cyclic loading force that is recorded by the servo-loading device. F_{\max} and F_{\min} are the maximum and the minimum force amplitudes recorded within the 100 cycles of the loading. Thus, ζ_b measures how close the cyclic loading force is from the ultimate bearing capacity F_u ; and ζ_c describes the extent of bearing-capacity reduction during the 100 cyclic loadings. The ratio between the maximum increments of the loading force and the loading displacement within one cycle is denoted as ζ_a , which has the physical meaning of secant stiffness of the force–displacement hysteretic loop.

4. Test Results of Model Pile–Bucket Foundation

In this section, the recorded horizontal loading force is plotted against the horizontal loading displacement to investigate the cyclic behavior of the model pile–bucket foundation.

4.1. Case One: Monotonic Loading

The horizontal force–displacement curve recorded at the loading point for case one, i.e., the monotonic loading case, is shown in Figure 8. The displacement is normalized respect to the pile diameter d . It is seen that the horizontal load increases linearly with the loading displacement initially. When the loading displacement exceeds about $0.13d$, the force–displacement plot becomes curved, which indicates that the soil surrounding the foundation begins to yield. Followingly, the yielding develops and the soil plastic zone expands, since a further decrease in the curve slope can be observed until the loading displacement reaches about $0.35d$. When the loading displacement grows from $0.35d$ to $1.4d$, the linear variation of the loading force over the displacement is regained, which indicates that the yielded soil enters into a strain-hardening state. The slope of the second linear section is only about 5% of the first one. Correspondingly, we state that the foundation–soil system is in the quasi-linear, yielding and strain-hardening states, respectively, when the loading displacement is in the ranges 0 – $0.13d$, $0.13d$ – $0.35d$ and $0.35d$ – $1.4d$. As suggested by Liu et al. [29], the horizontal load that reads from the reflection point on the force–displacement plot is taken as the ultimate bearing capacity, i.e., $F_u = 1563.2$ N.

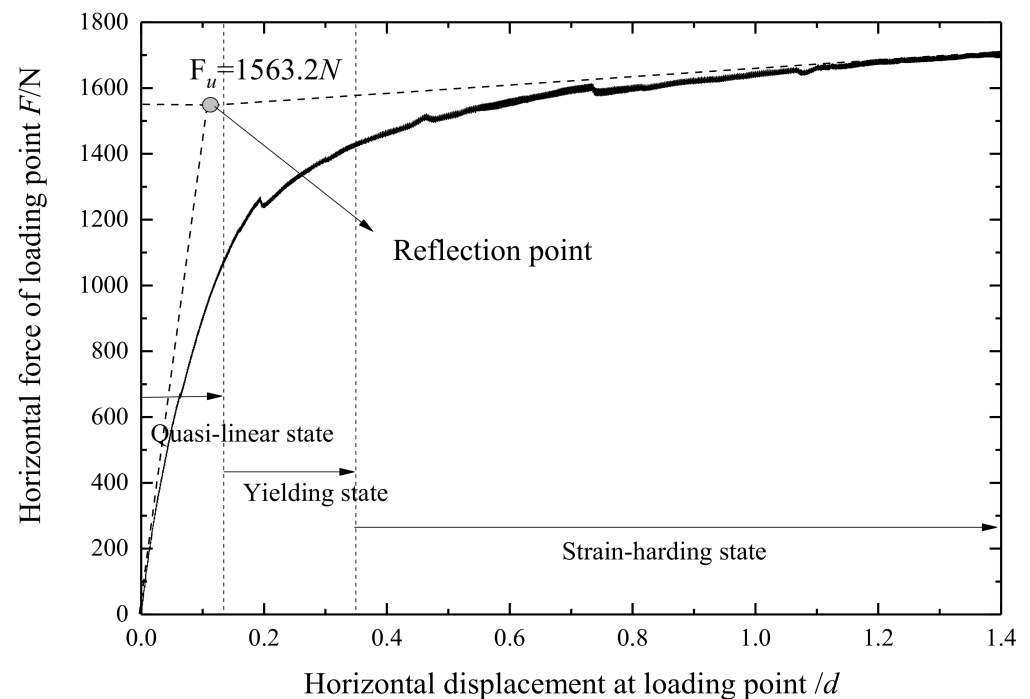


Figure 8. Variation of horizontal loading force with respect to horizontal displacement for monotonic loading case (case one).

4.2. Case Two: Cyclic Loading with Stepped Increasing Amplitudes

Five loading displacement amplitudes have been considered in this case (case two), while the typical wave loading frequency $f = 0.5$ Hz remains the same [30]. Take the displacement amplitude $A = \pm 5$ mm as an example, the recorded time variations of the horizontal loading force and displacement are presented in Figure 9a,b, respectively. Since the horizontal servo-loading device works in a displacement-controlled manner, the amplitudes of the horizontal displacement are well controlled to reach ± 5 mm during the entire 100 cycles, as shown in Figure 9a. However, for the horizontal loading force in Figure 9b, a gradual decrease in amplitude can be observed for the first 75 cycles, which indicates the stiffness degradation of the foundation–soil system. The system becomes stable for the remaining 25 cycles. From Figure 9b the maximum and the minimum absolute forces can be read as $F_{\max} = 485$ N and $F_{\min} = 405$ N, thus $\zeta_b = F_{\max}/F_u = 0.31$ and $\zeta_c = F_{\min}/F_{\max} = 0.83$ can be determined.

For the remaining four amplitudes, i.e., $A = \pm 10$, ± 20 , ± 25 and ± 30 mm, the time variations of the loading displacement and force follow a similar pattern as Figure 9. Thus, the plots are omitted to save the space. Table 4 summarizes the values of parameters ζ_b and ζ_c for all the five loading displacements.

It is read from the table that ζ_b gradually increases from 0.31 to 0.50 for the first three loading steps, then it reduces to 0.38 during the remaining two steps. While for ζ_c , an opposite variation with respect to the increasing amplitude can be observed.

To further explain the cyclic behavior, the variations of F_{\max} and F_{\min} have been added to Figure 8, which is redrawn in Figure 10. When the displacement is small, i.e., $A = 0.066d$, F_{\max} is close to the corresponding loading force read from the monotonic loading curve, which is within expectation since F_{\max} is determined from the 1st cycle. Limited stiffness degradation can be observed for the present loading amplitude since $\zeta_c = 0.83$. When the displacement amplitude increases further to $0.132d$ and then $0.263d$, more pronounced degradation can be observed as ζ_c reduces to 0.81 and 0.57, correspondingly. However, an increase in F_{\max} can still be observed, since the surrounding soil has been mobilized to a higher extent as per the enlarged displacement and the associated plastic zone in the soil.

It is noted that the foundation–soil system associated with $A = 0.263d$ is in the yielding state, as shown in Figure 10.

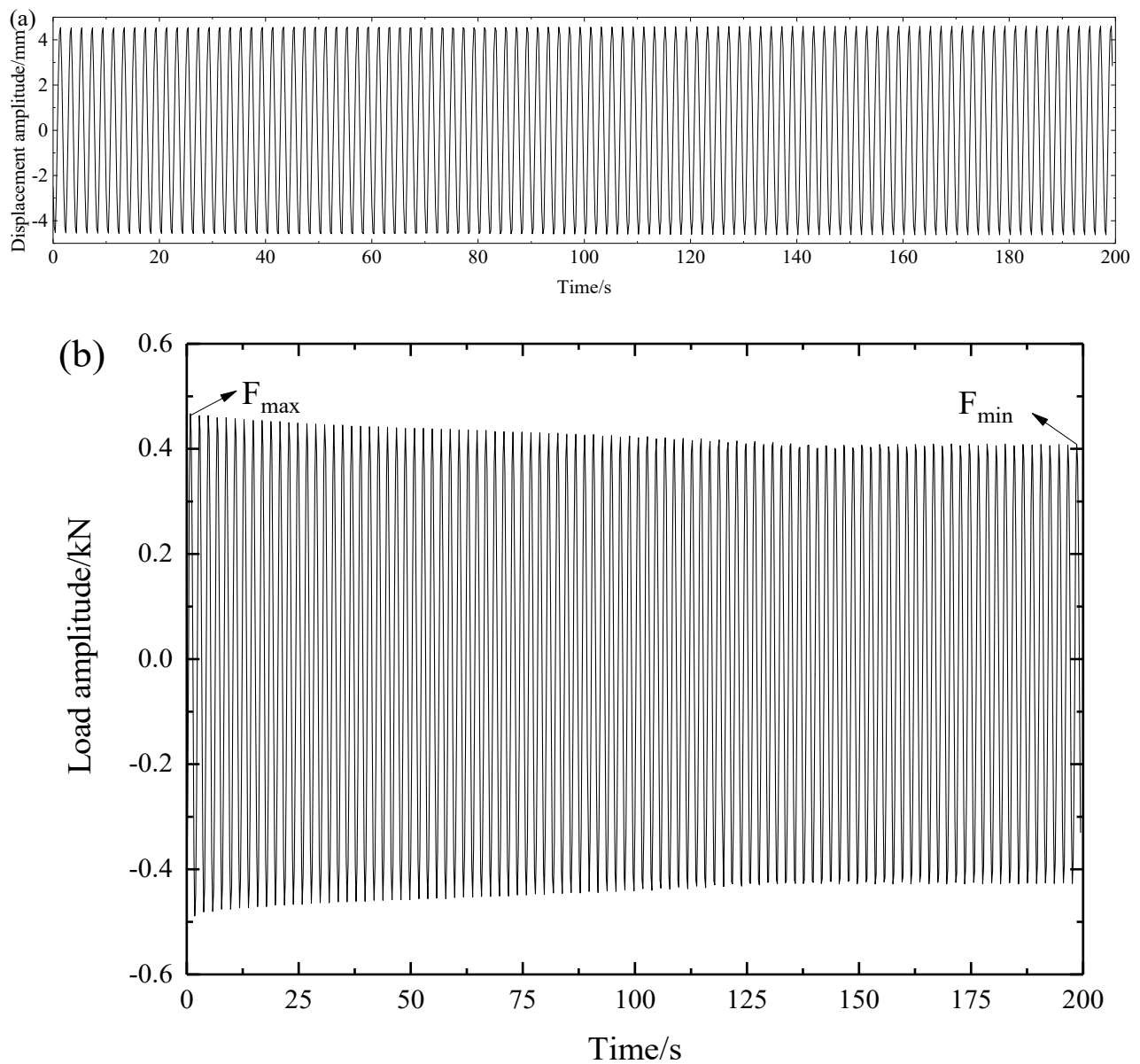


Figure 9. Variation of horizontal load with respect to time (a) horizontal loading displacement; (b) horizontal loading force.

Table 4. Parameters of loading forces corresponding to five displacement amplitudes.

Displacement Amplitude (mm)	Dimensionless Amplitude	Maximum Horizontal Force F_{\max} (N)	Minimum Horizontal Force F_{\min} (N)	$\zeta_b = F_{\max}/F_u$	$\zeta_c = F_{\min}/F_{\max}$
± 5	$0.066d$	485	405	0.31	0.83
± 10	$0.132d$	547	443	0.35	0.81
± 20	$0.263d$	781	449	0.50	0.57
± 25	$0.329d$	625	427	0.40	0.68
± 30	$0.394d$	594	478	0.38	0.80

Note: d is the pile diameter; F_u is the ultimate bearing capacity of the model foundation.

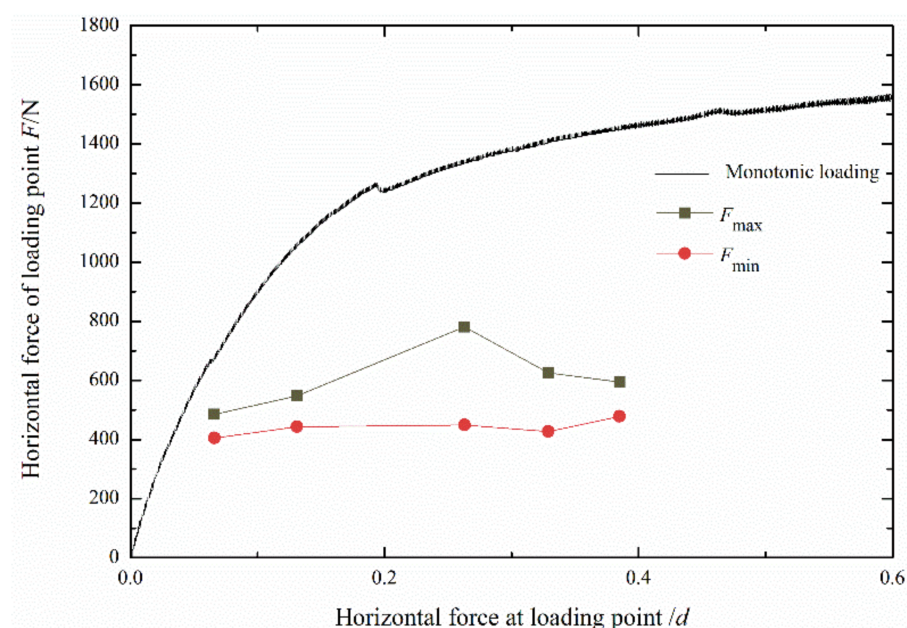


Figure 10. The maximum and minimum force amplitudes for the stepped-increasing displacement loading case of the model pile–bucket foundation.

The stiffness degradation is so obvious in the third loading step that the loading force can only be improved from $F_{\min} = 449$ N to $F_{\max} = 625$ N of the fourth loading step, even though a larger extent of the surrounding soil should have been mobilized when A increases from $0.263d$ to $0.329d$. However, less stiffness degradation is observed for the fourth loading step since ζ_c increases from 0.57 to 0.68, which indicates that the surrounding soil enters into the strain-hardening state after the yielding developed in the third step. Similar observations and explanations can be applied to the fifth loading step.

The variations of the horizontal loading forces over the horizontal displacements are presented in Figure 11, respectively, for the five amplitudes. To make the drawing clearer, the force–displacement curve is plotted only for the 1st–10th, 45th–55th and 90th–100th cycles for each displacement amplitude. All the force–displacement curves in Figure 11 form hysteretic loops. The area of the closed loop measures the damping effect of the foundation–soil system, and the slope of the loop backbone corresponds to the secant stiffness ζ_a .

The most significant degradation in the secant stiffness can be observed for $A = \pm 20$ mm (Figure 11c), when the amount of load cycling increases. While for the remaining figures, the degradation is not as pronounced as in Figure 11c. Especially when $A = \pm 5$ mm (Figure 11a), almost overlapping loops are observed for the total 100 cycles of loading. The observation keeps in line with the conclusion drawn from the variations of ζ_c as presented in Table 4, i.e., the stiffness degradation of the foundation–soil system will be most significant when the cyclic displacement amplitude is within the yielding range of the foundation–soil system (see Figure 8).

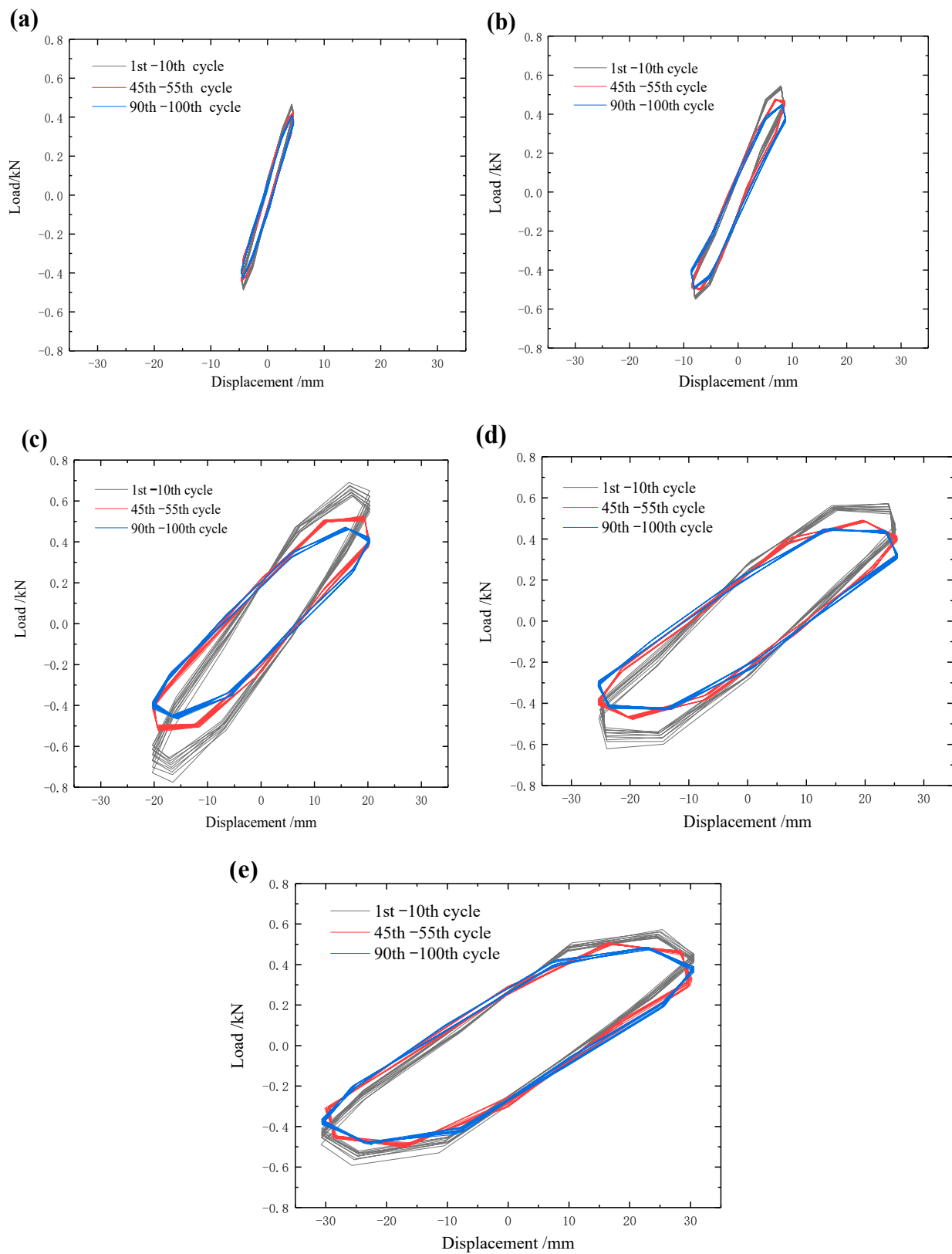


Figure 11. Variations of horizontal loading forces over horizontal loading displacements for five displacement amplitudes (case 2): (a) $A = \pm 5$ mm; (b) $A = \pm 10$ mm; (c) $A = \pm 20$ mm; (d) $A = \pm 25$ mm; (e) $A = \pm 30$ mm.

Additionally, a steady increase in the loop area can be observed when the displacement amplitude A increases from 5 to 30 mm, which means that the damping of the foundation–

soil system becomes more pronounced. The explanation is the ever-expanding plastic deformation zone in the surrounding soil along with the increasing displacement amplitude.

4.3. Case Three: Cyclic Loading with Stepped Increasing Frequency

In case three, the amplitude of the cyclic displacement loading is fixed to $A = \pm 2.5$ mm, while the cyclic frequency is increased in a stepped manner from 0.1 Hz to 0.5 Hz. The values of the parameters ζ_b and ζ_c that characterize the loading forces are summarized in Table 5.

Table 5. Parameters of loading forces corresponding to three cyclic frequencies.

Loading Frequency (Hz)	Maximum Horizontal Force F_{\max} (N)	Minimum Horizontal Force F_{\min} (N)	$\zeta_b = F_{\max}/F_u$	$\zeta_c = F_{\min}/F_{\max}$
0.1	656	487	0.42	0.74
0.3	481	385	0.31	0.80
0.5	275	262	0.18	0.95

Note: F_u is the ultimate bearing capacity of the model foundation.

For the influence of cycle numbers, it is found that $\zeta_c = 0.74$ is relatively large for $f = 0.1$ Hz, which means cumulative plastic deformation may have happened to the soil with increasing loading cycles. However, when f increases to 0.3 and 0.5 Hz, the number of repeated loadings has negligible influence on the stiffness degradation, since ζ_c increases to 0.8 and 0.95 for the two loading frequencies.

The variations of the horizontal loading forces over the horizontal displacements are presented in Figure 12, respectively, for the three cyclic frequencies. For the first frequency step, i.e., $f = 0.1$ Hz, the secant stiffness ζ_a of the hysteretic loop gradually decreases with increasing cycle number. Almost overlapping loops can be observed for the entire 100 cycles in Figure 12b,c, indicating that there is no cumulative plastic deformation to the soil within the current frequency step, i.e., $f = 0.3$ Hz or 0.5 Hz. These observations agree with those made from Table 5.

It is seen from Figure 12 that the loop area associated with the first frequency step is the largest, while the loop areas of the following two steps are almost the same. As can be seen from Table 5, F_{\max} associated with $f = 0.1$ Hz is the largest one among the three. The plastic deformation of the surrounding soil has adequately developed in the first step, i.e., the $f = 0.1$ Hz step. Thus, in the following two steps, i.e., $f = 0.3$ Hz and 0.5 Hz, there should be negligible plastic deformation happening to the soil. As a result, the damping of the last two steps generally remains the same.

As for the decreasing ζ_b with the increasing frequency observed both from Table 5 and Figure 12, it does not necessarily indicate stiffness degradation of the foundation–soil system. It may be the fact that irreversible plastic deformation has already happened to the surrounding soil during the previous frequency step. Consequently, for the following frequency step, smaller horizontal force needs to be applied since it only needs to overcome the elastic deformation out of the total displacement amplitude $A = \pm 2.5$ mm.

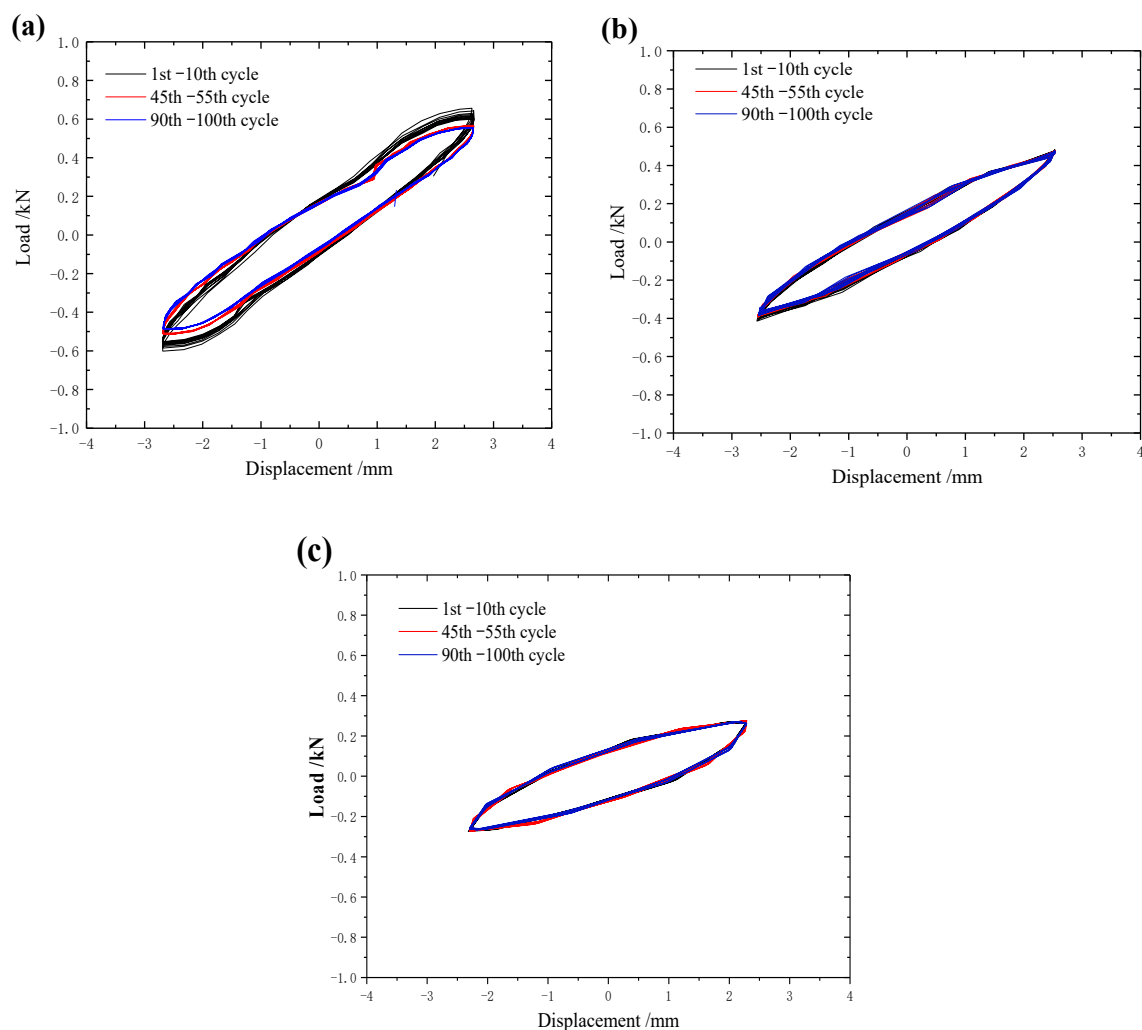


Figure 12. Variations of horizontal loading forces over horizontal loading displacements for three cyclic frequencies (case 3): (a) $f = 0.1$ Hz; (b) $f = 0.3$ Hz; (c) $f = 0.5$ Hz.

5. Discussion

The above sections present only directly measured data including the loading force and the loading displacement. Those direct data are processed herein to facilitate a deeper understanding of the cyclic loading effects. Through the strain gages distributed along the pile shaft, the tensile and compressive strains can be recorded for the model pile at the elevation of each gage pair. Then, the bending strain can be determined, and the resulting bending moment can be calculated by multiplying the bending strain with the predetermined bending rigidity $E_p I_p$. Take the first frequency step of case three as an example, i.e., $A = \pm 2.5$ mm and $f = 0.1$ Hz, the bending moment of the pile component of the pile–bucket foundation is presented in Figure 13.

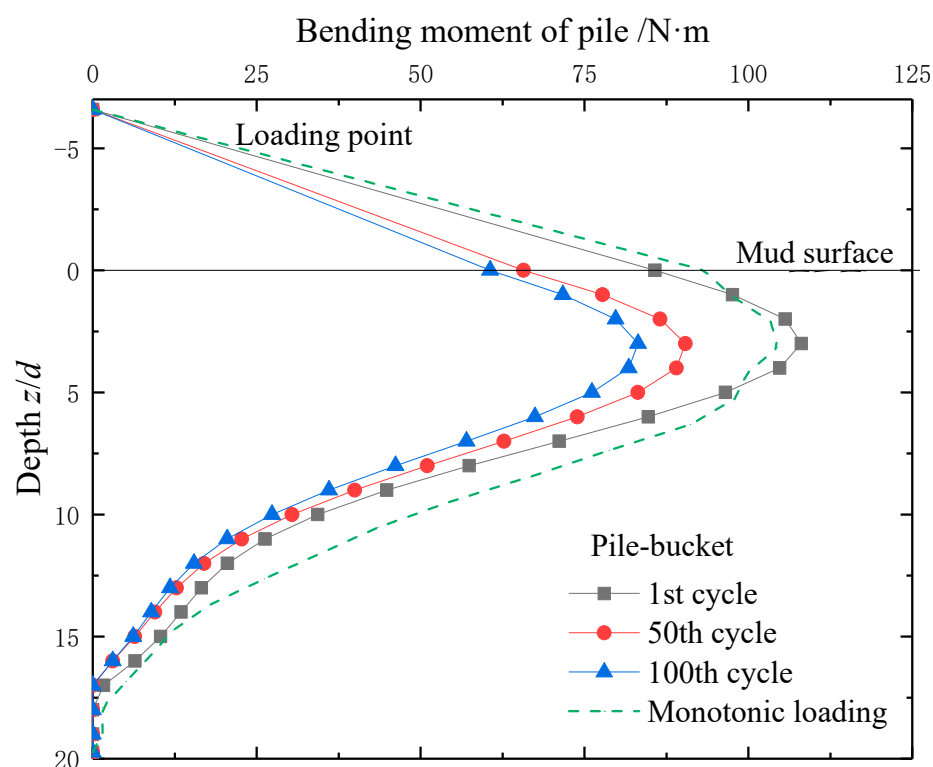


Figure 13. Bending moment of pile component of pile–bucket foundation when subjected to cyclic displacement loading of $A = \pm 2.5$ mm and $f = 0.1$ Hz.

It is seen that the bending moment distribution after the 1st cycle resembles that associated with the monotonic loading case. The reason for the stiffness degradation being not obvious is simply due to the fact that the displacement amplitude A is within the quasi-linear range of the foundation–soil system (see Figure 10). When the number of loading cycles increases to 50 and then to 100, an even decrease in the bending moment can be observed along the pile depth, i.e., the distribution pattern of the bending moment keeps while the peak value reduces. The reduction percentages of the peak bending moments read 18% and 8% for the 1st–50th cycle and the 50th–100th cycle, respectively.

Since the p (horizontal soil resistance)– y (horizontal pile displacement) method is widely adopted in the design practice of offshore wind-turbine foundations, the effects of cyclic loading are presented and discussed herein from the perspective of the p – y curve. First, the depth distribution of the bending moment of the model pile, as shown in Figure 13, is fitted into a polynomial of orders 6–8. Then, based on the beam bending theory completed by the displacement boundary conditions offered by the LVDTs (see Figure 2b), the depth distributions of the soil resistance (p) and the horizontal pile displacement (y) can be determined by performing differential and integral operations to the fitted polynomial with respect to the vertical coordinate.

The p – y curve evaluated at the depth $1d$ below the mud surface is shown in Figure 14 for the cyclic displacement loading with stepped increasing amplitudes, i.e., case two. The cyclic soil resistance p is normalized by dividing the ultimate soil resistance p_u determined from the monotonic loading case. The horizontal pile displacement y is normalized by dividing $y_c = 2.5 \times \varepsilon_c \times d$. Only the p – y curves corresponding to the 1st, 50th and 100th cycle of the stepped loading are drawn. All the p – y curves show a similar pattern, i.e., p grows quickly when y is small, and p approaches a stable value when y is sufficiently large. However, the increasing rate of p is decreased when the number of load cycles increases, e.g., the slope of the ascending section of the p – y curve associated with the 100th cycle is about 50% of that with the monotonic case.

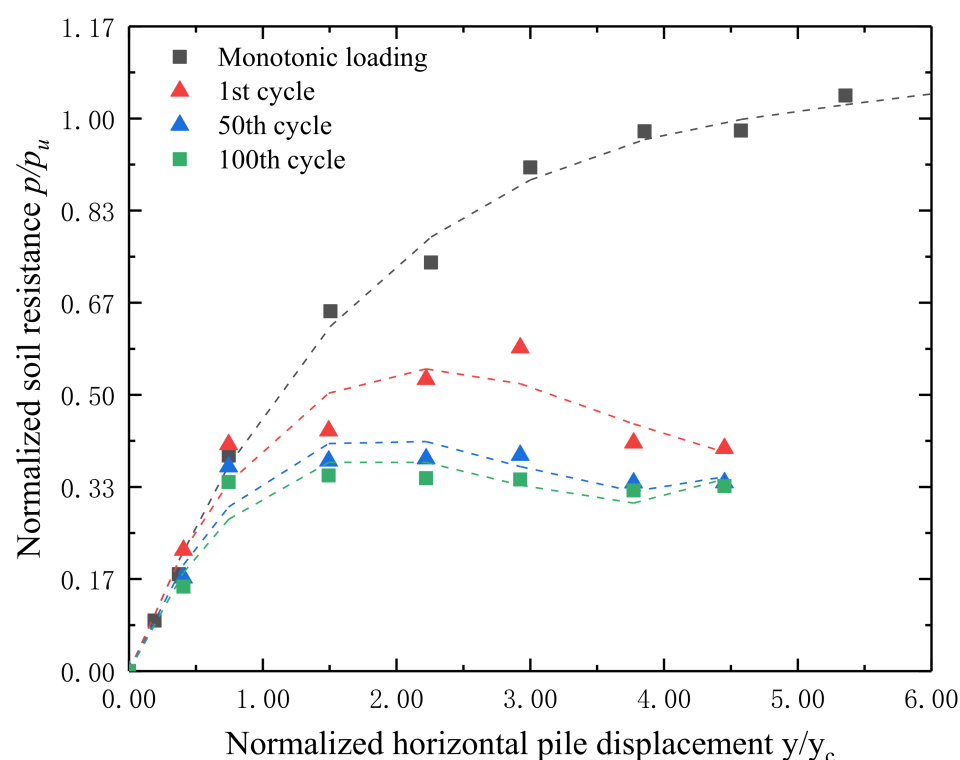


Figure 14. p – y curve evaluated 1d below mud surface for cyclic displacement loading with stepped increasing amplitude.

With the increasing loading cycles, it is observed from the p – y curves that the reduction of p becomes more obvious when the pile displacement y/y_c is larger than 1.4. Take $y/y_c = 2.8$ for example, the percentages of p reductions are 36%, 32% and 13% for the 0th–1st cycle, the 1st–50th cycle and the 50th–100th cycle, respectively. In this cyclic loading case, the ultimate soil resistance that is read from flat section of the p – y curve corresponding to the 100th cycle is about 33% of p_u . Thus, to obtain the cyclic p – y curve from the monotonic one, the above observations imply that significant reductions both in the slope and the ultimate soil resistance should be considered for the ascending and the flat sections of the monotonic p – y curve, respectively. It is noted that the cyclic ultimate soil resistance is suggested to be less than $0.72 p_u$ by the API code [31]. However, in the code no suggestion is given for the reducing the slope of the ascending section for the cyclic p – y curve.

6. Conclusions

A model test is designed and performed in this paper to investigate the cyclic horizontal load-bearing and deformation-resistance characteristics of the symmetric pile–bucket foundation embedded in soft marine clay. Three test cases have been conducted on the model foundation, i.e., the monotonic loading case and the cyclic horizontal-displacement loading cases either with stepped increasing amplitudes or with stepped increasing frequencies. The influences of cyclic loading parameters, including the amplitude, the frequency and the cycle number, have been studied from the perspective of stiffness-degradation and damping effect that are evaluated from the recorded horizontal force–displacement relationships at the loading point. Additionally, the influences of cyclic horizontal loading on the bending moment distribution and the p – y curve have been presented and discussed. The following conclusions can be drawn:

- (1) Under the displacement-controlled monotonic loading, the force–displacement curve of the pile–bucket foundation embedded in soft clay presents three distinct sections, i.e., the initial quasi-linear section, the following yielding section and the final strain-hardening section.

- (2) The stiffness degradation of the pile–bucket foundation will be most significant when the cyclic displacement amplitude is within the yielding range that is determined from the monotonic loading case. Furthermore, the damping of the foundation increases with the stepped-increasing amplitudes of the loading displacements, which indicates more soils surrounding the foundation have been mobilized.
- (3) Once the pile–bucket foundation has been subjected to cyclic displacement loadings with a low frequency, its stiffness and damping will basically not be affected by only increasing the loading frequency in the following loading cycles.
- (4) The stiffness degradation under the cyclic loadings will not affect the depth-distribution pattern of the pile bending moment. Additionally, the reductions of peak bending moment and soil resistance are more pronounced during the first few loading cycles.
- (5) To obtain the cyclic p – y curve from the monotonic case, significant reductions both in the slope (up to 50%) and the ultimate soil resistance (up to 67%) should be considered for the ascending and the flat sections of the monotonic p – y curve, respectively.

Author Contributions: Conceptualization, L.S. and Z.F.; methodology, L.S.; validation, Z.F., G.W. and Y.Y.; formal analysis, L.S.; investigation, Z.F.; data curation, Z.F.; writing—original draft preparation, Z.F.; writing—review and editing, L.S. All authors have read and agreed to the published version of the manuscript.

Funding: This research received no external funding.

Institutional Review Board Statement: Not applicable.

Informed Consent Statement: Not applicable.

Data Availability Statement: The data presented in the present study are available on request from the corresponding author. The data are not publicly available due to privacy concerns.

Conflicts of Interest: The authors declare no conflict of interest.

References

1. Wang, X.F.; Zeng, X.W.; Li, J.L.; Yang, X.; Wang, H.J. A review on recent advancements of substructures for offshore wind turbines. *Energy Convers. Manag.* **2018**, *158*, 103–119. [\[CrossRef\]](#)
2. Suleiman, M.T.; Ni, L.; Raich, A.; Helm, J.; Ghazanfari, E. Measured soil–structure interaction for concrete piles subjected to lateral loading. *Can. Geotech. J.* **2015**, *52*, 1168–1179. [\[CrossRef\]](#)
3. Li, W.; Zhu, B.T.; Yang, M. Static response of monopile to lateral load in overconsolidated dense sand. *J. Geotech. Geoenviron. Eng.* **2017**, *143*, 04017026. [\[CrossRef\]](#)
4. Yu, J.; Huang, M.S.; Leung, C.F.; Li, S. Upper bound solution of a laterally loaded rigid monopile in normally consolidated clay. *Comput. Geotech.* **2017**, *91*, 131–145. [\[CrossRef\]](#)
5. Zou, X.J.; Cao, X.; Zhou, C.L.; Zhou, M.; Mi, Z.; Zhang, X.H. Experimental study on the bearing capacity of large-diameter monopile in sand under water flow condition. *Ocean Eng.* **2021**, *224*, 108708. [\[CrossRef\]](#)
6. Leblanc, C.; Houlsby, G.T.; Byrne, B.W. Response of stiff piles in sand to long-term cyclic lateral loading. *Geotechnique* **2010**, *60*, 79–90. [\[CrossRef\]](#)
7. Zhang, C.; White, D.; Randolph, M. Centrifuge modeling of the cyclic lateral response of a rigid pile in soft clay. *J. Geotech. Geoenviron. Eng.* **2011**, *137*, 717–729. [\[CrossRef\]](#)
8. Lombardi, D.; Bhattacharya, S.; Dmw, C. Dynamic soil–structure interaction of monopile supported wind turbines in cohesive soil. *Soil Dyn. Earthq. Eng.* **2013**, *49*, 165–180. [\[CrossRef\]](#)
9. Yu, H.; Zeng, X.W.; Li, B.; Lian, J.J. Centrifuge modeling of offshore wind foundations under earthquake loading. *Soil Dyn. Earthq. Eng.* **2015**, *77*, 402–415. [\[CrossRef\]](#)
10. Hong, Y.; He, B.; Wang, L.Z.; Wang, Z.; Ng, C.W.W.; Masin, D. Cyclic lateral response and failure mechanisms of semi-rigid pile in soft clay: Centrifuge tests and numerical modelling. *Can. Geotech. J.* **2016**, *54*, 806–824. [\[CrossRef\]](#)
11. Liao, W.M.; Zhang, J.J.; Wu, J.B.; Yan, K.M. Response of flexible monopile in marine clay under cyclic lateral load. *Ocean Eng.* **2018**, *147*, 89–106. [\[CrossRef\]](#)
12. Lai, Y.Q.; Wang, L.Z.; Hong, Y.; He, B. Centrifuge modeling of the cyclic lateral behavior of large-diameter monopiles in soft clay: Effects of episodic cycling and reconsolidation. *Ocean Eng.* **2020**, *200*, 107048. [\[CrossRef\]](#)
13. Jawad, S.; Han, J.; Abdulrasool, G.; Al-Naddaf, M. Responses of single and group piles within mse walls under static and cyclic lateral loads. *Geotext. Geomembr.* **2021**, *49*, 1019–1035. [\[CrossRef\]](#)
14. Wang, X.F.; Yang, X.; Zeng, X.W. Centrifuge modeling of lateral bearing behavior of offshore wind turbine with suction bucket foundation in sand. *Ocean Eng.* **2017**, *139*, 140–151. [\[CrossRef\]](#)

15. Zhu, B.; Kong, D.Q.; Chen, R.P.; Kong, L.G.; Chen, Y.M. Installation and lateral loading tests of suction caissons in silt. *Can. Geotech. J.* **2011**, *48*, 1070–1084. [\[CrossRef\]](#)
16. Zhu, B.; Zhang, W.L.; Ying, P.P.; Chen, Y.M. Deflection-Based Bearing Capacity of Suction Caisson Foundations of Offshore Wind Turbines. *J. Geotech. Geoenviron. Eng.* **2014**, *140*, 04014013. [\[CrossRef\]](#)
17. Ma, P.C.; Liu, R.; Lian, J.J.; Zhu, B. An investigation into the lateral loading response of shallow bucket foundations for offshore wind turbines through centrifuge modeling in sand. *Appl. Ocean Res.* **2019**, *87*, 192–203. [\[CrossRef\]](#)
18. Cox, J.A.; O’Loughlin, C.D.; Cassidy, M.; Bhattacharya, S.; Gaudin, C.; Bienen, B. Centrifuge study on the cyclic performance of caissons in sand. *Int. J. Phys. Model. Geotech.* **2014**, *14*, 99–115. [\[CrossRef\]](#)
19. Foglia, A.; Ibsen, L.B. Monopod bucket foundation under cyclic lateral loading. *Int. J. Offshore Polar Eng.* **2016**, *26*, 109–115. [\[CrossRef\]](#)
20. Wang, L.Z.; Wang, H.; Hong, Y. Comparison of monotonic and cyclic lateral response between monopod and tripod bucket foundations in medium dense sand. *Ocean Eng.* **2018**, *155*, 88–105. [\[CrossRef\]](#)
21. Ueda, K.; Uzuoka, R.; Iai, S.; Okamura, T. Centrifuge model tests and effective stress analyses of offshore wind turbine systems with a suction bucket foundation subject to seismic load. *Soils Found.* **2020**, *70*, 1546–1569. [\[CrossRef\]](#)
22. Zhu, F.Y.; O’Loughlin, C.D.; Bienen, B.; Cassidy, M.J.; Morgan, N. The response of suction caissons to long-term lateral cyclic loading in single-layer and layered seabeds. *Géotechnique* **2018**, *68*, 729–741. [\[CrossRef\]](#)
23. Zhu, F.Y.; Bienen, B.; O’Loughlin, C.; Cassidy, M.J.; Morgan, N. Suction caisson foundations for offshore wind energy: Cyclic response in sand and sand over clay. *Géotechnique* **2019**, *69*, 924–931. [\[CrossRef\]](#)
24. Zhu, F.Y.; Bienen, B.; O’Loughlin, C.; Morgan, N.; Cassidy, M.J. The response of suction caissons to multidirectional lateral cyclic loading in sand over clay. *Ocean Eng.* **2018**, *170*, 43–54. [\[CrossRef\]](#)
25. Chen, D.; Gao, P.; Huang, S.S.; Li, C.S.; Yu, X.G. Static and dynamic loading behavior of a hybrid foundation for offshore wind turbines. *Mar. Struct.* **2020**, *71*, 102727. [\[CrossRef\]](#)
26. Head, K.H. *Manual of Soil Laboratory Testing: Soil Classification and Compaction Tests*, 2nd ed.; Pentech Press: London, UK, 1992.
27. Poulos, H.G.; Hull, T.S. The role of analytical geomechanics in foundation engineering. Presented at 1989 Foundation Engineering Conference, Evanston, IL, USA, 25–29 June 1989.
28. Zhang, Q.B.; Zhai, H.L.; Wang, P.D.; Wang, S.H.; Duan, L.L.; Chen, L.Y.; Liu, Y.F.; Jeng, D.S. Experimental study on irregular wave-induced pore-water pressures in a porous seabed around a mono-pile. *Appl. Ocean Res.* **2020**, *95*, 102041. [\[CrossRef\]](#)
29. Liu, R.; Li, B.R.; Lian, J.J.; Ding, H.Y. Bearing characteristics of pile-bucket composite foundation for offshore wind turbine. *J. Tianjin Univ. (Sci. Technol.)* **2016**, *48*, 429–437.
30. Arany, L.; Bhattacharya, S.; Macdonald, J.H.G.; Hogan, S.J. Closed form solution of Eigen frequency of monopile supported offshore wind turbines in deeper waters incorporating stiffness of substructure and SSI. *Soil Dyn. Earthq. Eng.* **2016**, *83*, 18–32. [\[CrossRef\]](#)
31. API. Recommended Practice for Planning, Designing and Constructing Fixed Offshore Platforms—Working Stress Design. Available online: <https://www.apiwebstore.org/publications/item.cgi?58bf26e5-8e94-4eb0-97f3-152abb4c1f37> (accessed on 1 June 2021).